



**Modelling the rheology of anisotropic particles adsorbed on
a two-dimensional fluid interface**

Journal:	<i>Soft Matter</i>
Manuscript ID:	SM-ART-02-2015-000372.R1
Article Type:	Paper
Date Submitted by the Author:	30-Mar-2015
Complete List of Authors:	Luo, Alan; ETH Zürich, Department of Materials Sagis, Leonard; Wageningen University, Öttinger, Hans Christian; ETH Zurich, Department of Materials De Michele, Cristiano; University of Rome "La Sapienza", Physics Ilg, Patrick; University of Reading, Mathematics and Statistics

Modelling the rheology of anisotropic particles adsorbed on a two-dimensional fluid interface

Alan M. Luo,^{*a} Leonard M. C. Sagis,^{ab} Hans Christian Öttinger,^a Cristiano De Michele,^c and Patrick Ilg^{ad}

Received Xth XXXXXXXXXX 20XX, Accepted Xth XXXXXXXXXX 20XX

First published on the web Xth XXXXXXXXXX 200X

DOI: 10.1039/b000000x

We present a general approach based on nonequilibrium thermodynamics for bridging the gap between a well-defined microscopic model and the macroscopic rheology of particle-stabilised interfaces. Our approach is illustrated by starting with a microscopic model of hard ellipsoids confined to a planar surface, which is intended to simply represent a particle-stabilised fluid-fluid interface. More complex microscopic models can be readily handled using the methods outlined in this paper. From the aforementioned microscopic starting point, we obtain the macroscopic, constitutive equations using a combination of systematic coarse-graining, computer experiments and Hamiltonian dynamics. Exemplary numerical solutions of the constitutive equations are given for a variety of experimentally relevant flow situations to explore the rheological behaviour of our model. In particular, we calculate the shear and dilatational moduli of the interface over a wide range of surface coverages, ranging from the dilute isotropic regime, to the concentrated nematic regime.

1 Introduction

Colloidal sized particles adsorbed onto a fluid-fluid interface enhances the interfacial rheological properties, leading to more stable foams and emulsions.¹ The particles tend to adsorb irreversibly and form a quasi-two dimensional microstructure on the interfaces, which prevents coalescence in foams and emulsions. Interestingly, the particle geometry seems to play an important role in the extent of enhancement of rheological properties. For example, elongated ellipsoidal colloids adsorbed onto an interface increase the values of the rheological properties more than their spherical counterparts, for an equal surface coverage.² Anisotropic particles are capable of forming more complex microstructures,^{3–5} due to the anisotropic nature of their interactions, with a more complex response to applied deformations.

These so-called particle-stabilised interfaces were first studied over a century ago^{6,7} but despite the wealth of experimental work there has so far been scant attention paid to theoretically modelling the surface rheology of these particle-stabilised interfaces.⁸ Certainly, these complex interfaces can be difficult to model due to the rich variety of interparticle

interactions such as interface-mediated capillary interactions and electrostatic interactions.^{9,10} In addition there can be curvature effects on particle motion¹¹ as well as a coupling between bulk and interface phases,¹² which can exchange mass, energy and momentum.

The system we envisage to model is that of a fluid-fluid interface with adsorbed anisotropic colloidal particles. Such a system can be rather complicated if one wishes to take into account all possible phenomena that can occur, therefore we make a number of simplifying assumptions: 1) The colloidal particles are hard, smooth, uncharged, ellipsoid-shaped and they move and lie in a two-dimensional solvent, which represents the interface. Furthermore, we assume that the interface is not deformed by the presence of these particles, which implies a 90 degree contact angle or sufficiently small nanometer scale particles.¹³ 2) The interface is assumed to be a planar surface, since many rheological experiments e.g. Langmuir troughs and bicone interfacial rheometers only measure flat interfaces. 3) The particles are adsorbed irreversibly due to large detachment forces for ellipsoidal particles at a fluid interface.¹⁴ 4) The system is homogeneous in temperature and particle surface coverage and induced flows do not induce gradients in concentration or in ordering. These idealisations essentially constitute our microscopic model, where we consider the interface as a two-dimensional bulk phase. We would, however, emphasise that our approach can handle systems where these idealisations are no longer valid. The fundamental requirement is a well-defined microscopic model.

We use the GENERIC (general equation for nonequilibrium

^a ETH Zürich, Department of Materials, Polymer Physics, CH-8093 Zürich, Switzerland.

^b Food Physics Group, Wageningen University, Bornse Weilanden 9, 6708 WG Wageningen, The Netherlands.

^c Dipartimento di Fisica, Università di Roma “La Sapienza”, Piazzale Aldo Moro 2, 00185 Roma, Italy.

^d School of Mathematical and Physical Sciences, University of Reading, Reading, RG6 6AX, United Kingdom.

reversible irreversible coupling) framework^{15–17} of nonequilibrium thermodynamics to systematically formulate the set of macroscopic equations of motion describing our system. Importantly, the GENERIC framework has a microscopic basis, which allows a systematic derivation of the macroscopic, continuum equations from a well-defined microscopic system.¹⁸ We are also able to link the time evolution of the microstructure to the applied deformation and recover an expression for the extra stress due to the microstructure, all formulated in a thermodynamically consistent manner. Since we have a microscopic basis for the macroscopic constitutive equations, we are able to capture the nonlinear rheology of our microscopic model over a range of particle surface coverages, from dilute to very concentrated. Our approach is rather general and can also be applied to modelling systems where some of the simplifications, such as the one concerning interparticle interactions, are no longer valid. We point out the necessary modifications to the methods we use in the appropriate sections.

This paper is organised in the following way. Section 2 briefly introduces the GENERIC framework we use for constructing the model. Section 3 concerns the systematic construction of the GENERIC building blocks and we obtain the constitutive equations from the microscopic model. Then the set of time evolution equations describing the model are summarised in Section 4, where we also discuss their behaviour under various flow conditions.

2 GENERIC framework

The GENERIC framework has been used as a tool for constructing thermodynamically consistent models for a multitude of different systems.¹⁵ Here we present a brief introduction to the framework. The first most crucial step is to identify the set of independent state variables $\mathbf{x}(\mathbf{r}, t)$ that are functions of position \mathbf{r} and time t that fully determine the system we wish to study at the chosen level of description. For brevity, we do not explicitly write out the position or time dependence of the state variables in the rest of this paper.

With the aforementioned simplifications in the Introduction, our system is described by the following set of independent state variables

$$\mathbf{x} = (\rho, \mathbf{M}, u, \eta, \mathbf{C}) \quad (1)$$

where ρ is the total mass density, \mathbf{M} is the total momentum density, u is the internal energy density of the fluid interface in the absence of adsorbed particles, η is a scalar describing the area fraction of the interface covered by particles and $\mathbf{C} = \langle \mathbf{u}\mathbf{u} \rangle$ is the orientation tensor with \mathbf{u} the two-dimensional orientation vector of a single particle, and $\langle \dots \rangle$ denotes an ensemble average. The variables η and \mathbf{C} together describe the structure of the interface and density is understood to mean an area density. In principle, a proper thermo-

dynamic treatment of a dividing interface *à la* Gibbs requires excess densities, which may depend on the choice of gauge defining the position of the interface.¹⁹ In this paper, we simplify matters by treating the interface as a two-dimensional bulk phase.

The time evolution of the set of state variables is then given by the equation

$$\dot{\mathbf{x}} = L \cdot \frac{\delta E}{\delta \mathbf{x}} + M \cdot \frac{\delta S}{\delta \mathbf{x}}, \quad (2)$$

where $\delta/\delta \mathbf{x}$ denotes functional derivatives, L is the Poisson matrix and E is the total energy; together they describe the reversible dynamics. M is the friction matrix and together with the entropy S gives the irreversible dynamics. The GENERIC equation (2) can be written equivalently in terms of brackets

$$\dot{A} = \{A, E\} + [A, S], \quad (3)$$

where A is an arbitrary functional of the state variables. The Poisson bracket is defined as

$$\{B, C\} = \int \frac{\delta B}{\delta \mathbf{x}} \cdot L \cdot \frac{\delta C}{\delta \mathbf{x}} d^2 r \quad (4)$$

where B, C are also arbitrary functionals of the state variables. The underlying Poisson geometric structure imposes certain conditions on the Poisson bracket, namely antisymmetry $\{A, B\} = -\{B, A\}$, the Leibniz rule $\{AB, C\} = A\{B, C\} + B\{A, C\}$ and Jacobi identity $\{A, \{B, C\}\} + \{B, \{C, A\}\} + \{C, \{A, B\}\} = 0$. The dissipative bracket is defined as

$$[B, C] = \int \frac{\delta B}{\delta \mathbf{x}} \cdot M \cdot \frac{\delta C}{\delta \mathbf{x}} d^2 r. \quad (5)$$

It is less constrained than the Poisson bracket and simply has the properties of symmetry $[A, B] = [B, A]$ and positive semi-definiteness $[A, A] \geq 0$, which ensures that entropy production is non-negative for irreversible dynamics. There are two supplementary degeneracy conditions

$$\{A, S\} = 0, \quad (6)$$

$$[A, E] = 0 \quad (7)$$

which together ensure that total energy is conserved $\dot{E} = 0$ and total entropy production is non-negative $\dot{S} = [S, S] \geq 0$, therefore guaranteeing thermodynamic consistency. In addition, the first degeneracy condition implies reversible dynamics are entropy conserving.

So to construct a model using the GENERIC framework requires us to specify the four building blocks L, M, E, S . Crucially, all of the building blocks can be formulated using a statistical approach (coarse-graining) of the microscopic system.¹⁸ We use this statistical approach to help formulate the entropy functional S and the friction matrix M .

3 Constructing the constitutive model

In this section we systematically formulate the four building blocks of GENERIC. In contrast to an earlier model,²⁰ the formulation presented in this paper is based on and derived from a microscopic model.

3.1 Energy and entropy

Two of the building blocks in the GENERIC framework are the energy and entropy functionals. We model the adsorbed colloidal particles as hard ellipsoidal particles confined to a two-dimensional plane, and the interface as a viscous (two-dimensional) fluid. Therefore there is no particle-particle interaction energy and we can write the energy functional as

$$E = \int \left(\frac{M^2}{2\rho} + u \right) d^2r. \quad (8)$$

Recall that the state variables are dependent on position so that *e.g.* the internal energy density of the fluid u is equal to zero where particles are present. Thus the surface coverage is implicitly taken into account in the integral. The entropy is

$$S = \int s(\rho, u, \eta, \mathbf{C}) d^2r. \quad (9)$$

We assume the entropy density per unit area s can be split into separate contributions from the solvent s_s , and from the structure formed by the ellipses. The structural entropy can be further decomposed into an ideal part s_{id} associated with the entropy of an ensemble of non-interacting rotators, and an excess part s_{excl} associated with excluded volume interactions between our hard ellipses. Therefore we write

$$s = s_s(\rho, u) + s_{id}(\eta, \mathbf{C}) + s_{excl}(\eta, \mathbf{C}). \quad (10)$$

The latter two contributions have been determined²¹ to be

$$s_{id} = k_B n_p \left[\frac{1}{2} \ln(1 - S_2) + \frac{1}{2} S_2 - \frac{3}{4} (S_2)^2 + \frac{1}{6} (S_2)^3 - \frac{1}{8} (S_2)^4 + \frac{1}{10} (S_2)^5 - \frac{1}{18} (S_2)^6 \right] \quad (11)$$

$$s_{excl} = k_B n_p (\eta + a\eta^2) [b(S_2)^2 + c(S_2)^4] \quad (12)$$

where $S_2 = \sqrt{2\mathbf{C} : \mathbf{C} - 2\text{tr}\mathbf{C} + 1}$ is an order parameter that varies from 0 in the isotropic phase to 1 in the perfectly ordered phase, n_p is the number density of particles adsorbed on the interface (related to the surface coverage by $A_p n_p = \eta$, where A_p is the interfacial area removed by a single particle) and $a = 2.107, b = 0.654, c = 0.175$ are numerical parameters for ellipses with an aspect ratio $k = 4$. For other aspect ratios or particle geometries, a systematic procedure^{21,22} can be applied to determine a coarse-grained free energy. The

entropy of mixing has been neglected as we have begun by assuming a homogeneous surface coverage. Functional derivatives of the energy and entropy are respectively

$$\frac{\delta E}{\delta \mathbf{x}} = \begin{pmatrix} -\frac{v^2}{2} \\ \mathbf{v} \\ 1 \\ 0 \\ 0 \end{pmatrix} \quad \text{and} \quad \frac{\delta S}{\delta \mathbf{x}} = \begin{pmatrix} -\frac{\mu}{T} \\ 0 \\ \frac{1}{T} \\ \frac{\partial s}{\partial \eta} \\ \frac{\partial s}{\partial \mathbf{C}} \end{pmatrix} \quad (13)$$

where the velocity is defined as $\mathbf{v} = \mathbf{M}/\rho$, the temperature is $T = (\frac{\partial s}{\partial u})^{-1}$ and μ is the chemical potential for the solvent. For completeness, the remaining derivatives in the functional derivative of the entropy are

$$\frac{\partial s}{\partial \eta} = \frac{s_{id}}{A_p} + k_B n_p (2 + 3a\eta) [b(S_2)^2 + c(S_2)^4], \quad (14)$$

$$\frac{\partial s}{\partial \mathbf{C}} = k_B n_p f(\eta, S_2) (\mathbf{C} - \frac{1}{2} \boldsymbol{\delta}), \quad (15)$$

where $\boldsymbol{\delta}$ is the 2×2 identity matrix and

$$f(\eta, S_2) = \frac{2(S_2)^5 - 5(S_2)^4 + 6(S_2)^3 - 6(S_2)^2 + 12S_2 - 12}{3(1 - S_2)} + 4(\eta + a\eta^2)(b + 2c(S_2)^2). \quad (16)$$

3.2 Poisson bracket

The Poisson bracket gives the reversible dynamics and can be formulated as

$$\begin{aligned}
\{A, B\} = & - \int \rho \left(\frac{\delta A}{\delta M_j} \frac{\partial}{\partial r_j} \frac{\delta B}{\delta \rho} - \frac{\delta B}{\delta M_j} \frac{\partial}{\partial r_j} \frac{\delta A}{\delta \rho} \right) d^2 r \\
& - \int M_k \left(\frac{\delta A}{\delta M_j} \frac{\partial}{\partial r_j} \frac{\delta B}{\delta M_k} - \frac{\delta B}{\delta M_j} \frac{\partial}{\partial r_j} \frac{\delta A}{\delta M_k} \right) d^2 r \\
& - \int u \left(\frac{\delta A}{\delta M_j} \frac{\partial}{\partial r_j} \frac{\delta B}{\delta u} - \frac{\delta B}{\delta M_j} \frac{\partial}{\partial r_j} \frac{\delta A}{\delta u} \right) d^2 r \\
& - \int s_{jk} \left(\frac{\delta A}{\delta u} \frac{\partial}{\partial r_j} \frac{\delta B}{\delta M_k} - \frac{\delta B}{\delta u} \frac{\partial}{\partial r_j} \frac{\delta A}{\delta M_k} \right) d^2 r \\
& + \int C_{jk} \frac{\partial}{\partial r_l} \left(\frac{\delta A}{\delta C_{jk}} \frac{\delta B}{\delta M_l} - \frac{\delta B}{\delta C_{jk}} \frac{\delta A}{\delta M_l} \right) d^2 r \\
& + \int C_{lk} \left(\frac{\delta A}{\delta C_{jk}} \frac{\partial}{\partial r_l} \frac{\delta B}{\delta M_j} - \frac{\delta B}{\delta C_{jk}} \frac{\partial}{\partial r_l} \frac{\delta A}{\delta M_j} \right) d^2 r \\
& + \int C_{jl} \left(\frac{\delta A}{\delta C_{jk}} \frac{\partial}{\partial r_l} \frac{\delta B}{\delta M_k} - \frac{\delta B}{\delta C_{jk}} \frac{\partial}{\partial r_l} \frac{\delta A}{\delta M_k} \right) d^2 r \\
& - \int 2C_{ij} C_{kl} \left(\frac{\delta A}{\delta C_{ij}} \frac{\partial}{\partial r_l} \frac{\delta B}{\delta M_k} - \frac{\delta B}{\delta C_{ij}} \frac{\partial}{\partial r_l} \frac{\delta A}{\delta M_k} \right) d^2 r \\
& - \int \eta \left(\frac{\delta A}{\delta M_j} \frac{\partial}{\partial r_j} \frac{\delta B}{\delta \eta} - \frac{\delta B}{\delta M_j} \frac{\partial}{\partial r_j} \frac{\delta A}{\delta \eta} \right) d^2 r, \quad (17)
\end{aligned}$$

where we use the Einstein summation convention for the indices i, j, k, l . The first four integrals form the usual Poisson bracket of hydrodynamics^{15,23} with a stress tensor \mathbf{s} determined by the degeneracy condition $\{A, S\} = 0$, giving

$$\begin{aligned}
\mathbf{s} = T \left[\left(s - \rho \frac{\partial s}{\partial \rho} - u \frac{\partial s}{\partial u} - \eta \frac{\partial s}{\partial \eta} \right) \boldsymbol{\delta} \right. \\
\left. + 2\mathbf{C} \cdot \frac{\partial s}{\partial \mathbf{C}} - 2 \left(\mathbf{C} : \frac{\partial s}{\partial \mathbf{C}} \right) \mathbf{C} \right]. \quad (18)
\end{aligned}$$

This expression for the stress can be identified with the expression given by Edwards *et al.*²⁴ We are further able to identify the surface tension γ as

$$\gamma = u - Ts - \rho\mu + \eta T \frac{\partial s}{\partial \eta}, \quad (19)$$

with the contribution to the surface stress due to the structural variables given by

$$\mathbf{\Pi} = 2T \left[\mathbf{C} \cdot \frac{\partial s}{\partial \mathbf{C}} - \left(\mathbf{C} : \frac{\partial s}{\partial \mathbf{C}} \right) \mathbf{C} \right], \quad (20)$$

so the reversible contribution to the surface stress can be written as

$$\mathbf{s} = -\gamma \boldsymbol{\delta} + \mathbf{\Pi}. \quad (21)$$

The next four integrals in Eq. (17) represent upper convective behaviour for the tensor variable, with the integral involving the term $2C_{ij}C_{kl}$ required to preserve the trace of \mathbf{C} .^{24,25} The final integral describes the convection of the particle surface coverage η . And we note that the Jacobi identity is satisfied for our bracket Eq. (17).²⁶

3.3 Friction matrix

There are two dissipative processes that can occur in our model: viscous heating and rotational relaxation of the particles. We treat viscous heating first, followed by rotational relaxation. Friction matrix entries for other possible dissipative processes that we have neglected such as diffusion in the presence of gradients of the structural variables, or temperature, are well-known.^{12,15}

3.3.1 Surface viscosity. This is the usual hydrodynamics entry for a viscous fluid specialised to a surface,¹² which is

$$\begin{aligned}
[A, B]_{\text{hydro}} = & \int 2\varepsilon_s T \left(\frac{\overline{\partial}}{\partial r_i} \frac{\delta A}{\delta M_j} - \dot{\gamma}_{ij} \frac{\delta A}{\delta u} \right) \left(\frac{\overline{\partial}}{\partial r_i} \frac{\delta B}{\delta M_j} - \dot{\gamma}_{ij} \frac{\delta B}{\delta u} \right) d^2 r \\
& + \int \varepsilon_d T \left(\frac{\partial}{\partial r_i} \frac{\delta A}{\delta M_i} - \dot{\gamma}_{ii} \frac{\delta A}{\delta u} \right) \left(\frac{\partial}{\partial r_j} \frac{\delta B}{\delta M_j} - \dot{\gamma}_{jj} \frac{\delta B}{\delta u} \right) d^2 r \quad (22)
\end{aligned}$$

where ε_s is the surface shear viscosity, ε_d is the surface dilational viscosity and $\dot{\gamma} = \frac{1}{2}(\boldsymbol{\kappa} + \boldsymbol{\kappa}^T)$ is the symmetrised velocity gradient tensor, with $\boldsymbol{\kappa} = \partial \mathbf{v} / \partial \mathbf{r}$. A bar over a tensor indicates that we are only considering the traceless, symmetric part of that tensor.

3.3.2 Rotational relaxation. In this section the friction matrix entry for the tensor variable \mathbf{C} is determined for a range of packing fractions for the particular aspect ratio $k = 4$. We use a mixture of analytic results and computer simulations to guide the formulation of this entry.

In its simplest form, the friction matrix entry for relaxation of \mathbf{C} to equilibrium would be a constant inverse relaxation time.²⁷ In the related case of polymer melts, it was found that the friction matrix depends on the structural state variables.²⁸ We begin by looking at the microscopic system, which is modelled using hard ellipsoids. Then a Green-Kubo relation relates the fluctuations of \mathbf{C} to its relaxation dynamics¹⁵

$$M_{\text{rot}} = \frac{1}{k_B} \int_0^{\tau_s} \langle \dot{\mathbf{C}}^f(t) \dot{\mathbf{C}}^f(0) \rangle dt, \quad (23)$$

where $\dot{\mathbf{C}}^f$ are the fast fluctuations of the variable \mathbf{C} and τ_s is an intermediate separating timescale between fast dynamics (unresolved on the macroscopic level and which we regard as

noise), and the slow dynamics of our state variables. The state variables should not change systematically on the timescale τ_s . This approach was demonstrated successfully to obtain the friction matrix numerically²⁹ and semi-analytically²⁸ for the case of polymer melts. To include other inter-particle interactions, it suffices to use the appropriate interaction potential in the computer simulations.

We note that the average in Eq. (23) should, in principle, be taken at equilibrium or where there exists an appropriate distribution function describing the out-of-equilibrium state. Hence Eq. (23) may not necessarily be valid in *all* nonequilibrium situations. However, in this particular case, we benefit from the isotropic-nematic transition, giving us access to equilibrium states with non-zero ordering $C \neq \delta/2$ and we further benefit from the symmetry of C , which has only one tensorial invariant. Therefore flow does not lead to a different tensor structure (which would break the symmetry).

If we make the assumption that the fast rotational dynamics of a single ellipsoid is described by Brownian motion, we can formulate an analytic expression with only one unknown parameter. Detailed calculations leading to the result Eq. (24) are presented in the Appendix. Whether the Brownian motion is caused by multiple collisions between colloid particles, or by thermal fluctuations of the solvent is unimportant; the only parameter is the rotational relaxation timescale τ_{rot} . The theoretical result is

$$(M_{\text{rot}})_{ijkl} = \frac{1}{k_B n_p \tau_{\text{rot}}} (C_{ik} \delta_{jl} + C_{jk} \delta_{il} + C_{jl} \delta_{ik} + C_{il} \delta_{jk} - 4(C_4)_{ijkl}), \quad (24)$$

where $(C_4)_{ijkl} = \langle u_i u_j u_k u_l \rangle$ is the fourth moment of the orientation distribution, which arises due to the inextensibility of the particles. It can be expressed exactly in terms of second rank tensors and the order parameters S_2 and S_4 in the two-dimensional case, see Eq. (47) in the Appendix. The order parameters are given by $S_2 = \langle \cos 2\theta \rangle$ and $S_4 = \langle \cos 4\theta \rangle$, where θ is the angle between a particle's orientation vector and the director, which is the average orientation of all the particles. Our exact expression for $(C_4)_{ijkl}$ is rather lengthy so we provide it in the Appendix.

The values of the individual components $(M_{\text{rot}})_{ijkl}$ can be matched to those of the tensor in Eq. (23) obtained numerically via equilibrium molecular dynamics simulations. There is then a single fitting parameter, the rotational timescale τ_{rot} , allowing a relationship between τ_{rot} and η to be established. The computer simulations we use to verify the tensor structure of Eq. (24) and to help guide development of the friction matrix are event-driven molecular dynamics (EDMD).³⁰ Note that since we simulate hard ellipsoids-of-revolution confined to a plane, the moment of inertia I is different compared to a true two-dimensional ellipse. The temperature of the system is set to $k_B T = 1$; equipartition then sets the intrinsic units of

time in the simulation. Explicitly, time is measured in our simulations in units of $\tilde{\tau} = (1/2\pi)\sqrt{I/k_B T}$. There is no solvent in these simulations to save on computational complexity and efficiency.

The existence of τ_s is crucial to obtaining a meaningful friction matrix from simulations, therefore a small discussion of the various rotational timescales in our model is appropriate. Thinking about the model when there is a solvent present, the rotational dynamics of the colloidal particles is due to Brownian motion and collisions with other colloids, which introduces two timescales: an intrinsic time for the rotation of a single particle τ_{rot} , and the average time between collisions τ_{coll} . It is expected and verified by our computer simulations that τ_{coll} decreases monotonically with η , see Figure 1. We also consider that τ_{rot} is approximately constant for dilute systems because there are few collisions and changes of orientation are caused primarily by solvent thermal fluctuations. Then τ_{rot} should diverge as the nematic phase and close packing limit is approached since it becomes increasingly difficult for the ellipses to reorientate due to caging effects.

In our EDMD simulations, the origin of the ‘‘noise’’ is exclusively due to multiple collisions between the ellipsoids, like in the kinetic theory of gases. The validity of a thermodynamic description requires that there is a clear separation of timescales between the fast processes (‘‘noise’’) and systematic changes of the state variables. Therefore we can only use Eq. (23) to construct M when the two timescales τ_{rot} and τ_{coll} are sufficiently separated *i.e.* when $\tau_{\text{rot}} \gg \tau_{\text{coll}}$.

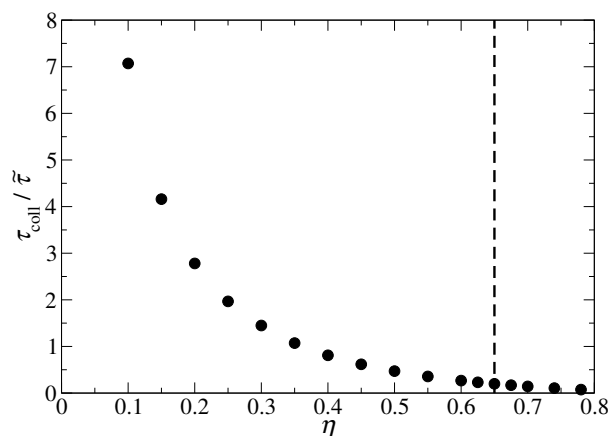


Fig. 1 The average time between collisions as a function of surface coverage fraction. The vertical dashed line represents the approximate position of the isotropic-nematic transition for aspect ratio 4 ellipses.²¹ The estimated uncertainty is smaller than the symbol size.

3.3.2.1 Isotropic state. For intermediate values of the surface coverage when the equilibrium state is isotropic, there is

no range of intermediate timescales τ_s where M is approximately independent of τ_s , making it impossible to use Eq. (23). Indeed, this is symptomatic of cases where there is no clear separation between “fast” and “slow” dynamics. In this range of area fractions we have that $\tau_{\text{coll}} \approx \tau_{\text{rot}}$. We note that previous studies of the force autocorrelation function of Brownian particles suggested to choose the separating timescale τ_s to be when the autocorrelation function crosses zero for the first time³¹ or to fit the (time-dependent) friction to an exponential decay form, and associate the decay constant with the friction coefficient.³² However, we try a different approach outlined below, which we find gives more reliable results for our case.

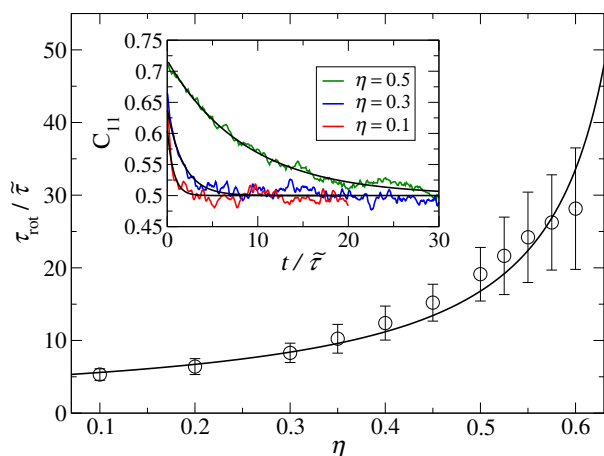


Fig. 2 Time constant of Eq. (26) as a function of surface coverage. It is shown with a power law fit Eq. (27) that diverges as jamming is approached (solid black line). *Inset:* Relaxation of the C_{11} tensor component. Initially the system is put into a partially ordered state and we follow its evolution to the equilibrium isotropic state. The remaining independent off-diagonal tensor component is initially set to zero and remains zero.

Begin by noting that the friction matrix must be an isotropic rank-4 tensor close to the equilibrium isotropic phase due to symmetry requirements. Take the isotropic limit of Eq. (24) to obtain

$$\lim_{\substack{S_2, S_4 \rightarrow 0 \\ \mathbf{C} \rightarrow \delta/2}} (M_{\text{rot}})_{ijkl} = \frac{1}{2k_{\text{B}}n_{\text{p}}\tau_{\text{rot}}} (\delta_{jk}\delta_{il} + \delta_{ik}\delta_{jl} - \delta_{ij}\delta_{kl}). \quad (25)$$

Since, close to equilibrium the entropy gradient is a linear function of \mathbf{C} , and the irreversible dynamics is given by Eq. (25) double contracted with the entropy gradient, we expect a time evolution equation with an exponential decay solution containing one time constant

$$\mathbf{C}(t) = \mathbf{C}(0)e^{-t/\tau} + \frac{1}{2}\delta. \quad (26)$$

where $1/\tau = 4[b(\eta + a\eta^2) - 1]/\tau_{\text{rot}}$ is the decay constant,

which is related to the rotational timescale. To test this reasoning, we perform computer experiments, in which the initial state is out of equilibrium, and we watch how the components of \mathbf{C} relax to their equilibrium values. To construct the initial configurations, Monte-Carlo simulations of $N = 2025$ ellipsoids in the generalised canonical ensemble are performed, where Lagrange multipliers are used to specify the average orientation. The initial states have surface coverages which have an isotropic equilibrium state, but are held in a nonequilibrium ordered state by the Lagrange multipliers. For each packing fraction we generate 150 independent initial configurations and use our EDMD code to observe the time series of the orientation tensor components as the configurations equilibrate. An exponential decay fits our data rather well, from which we extract the time constant τ_{rot} for various surface coverages, see Figure 2. Taking inspiration from the slowing down of dynamics observed as granular materials approach jamming, we fit the decay constant with a power law

$$\tau_{\text{rot}} = \tau_{\text{visc}} |1 - \eta/\eta_{\text{J}}|^{-1}, \quad (27)$$

where the fitting parameters are: $\tau_{\text{visc}} = 4.80 \pm 0.40$ and $\eta_{\text{J}} = 0.70 \pm 0.04$. The parameter τ_{visc} is the rotational timescale of an ellipsoid in the limit of zero surface coverage and this could be determined experimentally by observing the motion of a single adsorbed particle. We propose that η_{J} is the maximal surface coverage that could be obtained by a *random* packing of ellipses. However, this divergence of the relaxation time cannot be observed because the isotropic-nematic phase transition occurs at a surface coverage $\eta_{\text{in}} \sim 0.65$,²¹ before the system can become jammed.

3.3.2.2 Nematic state. Now we discuss the case when there is a clear separation of timescales, for example in the nematic phase ($\eta > \eta_{\text{in}}$) when the relaxation of \mathbf{C} is slow compared to the microscopic timescale. Then there exists a plateau region where the entries of M are approximately constant. This region exists between the fast collision timescale and the slow time for rotation of a particle $\tau_{\text{coll}} \ll \tau_s \ll \tau_{\text{rot}}$. We perform equilibrium EDMD simulations of the hard ellipsoids for various surface coverages in order to calculate the friction matrix entry using the Green-Kubo type formula of Eq. (23). Note that it is necessary to average over many independent trajectories in order to calculate the correlation function in Eq. (23) sufficiently accurately. Some examples of M_{rot} extracted from simulations are shown in Figure 3, where a plateau region is clearly visible. We can therefore extract a value for each tensor component of M_{rot} by taking its mean value in the range $\tau_s \in [20, 50]$. Comparison of this with the analytic expression for M_{rot} yields the rotational timescale τ_{rot} . We take the simulation values for $S_2, S_4, \mathbf{C}, \mathbf{C}_4$ to use in the analytic expression Eq. (24). Importantly, the tensor structure of M_{rot} in Eq. (24) is confirmed by our simulations.

The rotational timescale as a function of the surface coverage for the nematic phase can once again be nicely fitted using a power law $\tau_{\text{rot}} = \tau_{\text{nem}}|1 - \eta/\eta_{\text{max}}|^{-\beta}$ with a dynamical critical exponent $\beta = 4.88 \pm 0.02$ and intrinsic timescale $\tau_{\text{nem}} = (1.11 \pm 0.20) \times 10^2$. The fit diverges at a significantly higher surface coverage $\eta_{\text{max}} = \pi/\sqrt{12}$. This is the maximum possible surface coverage,³³ where the ellipses are arranged regularly on a lattice and kinetically arrested – at this very high surface coverage there is no movement possible of the particles without causing an overlap.

The additional parameter τ_{nem} is significantly greater than the viscous rotational time τ_{visc} because in the nematic phase, rotation of a single particle requires a collective rotation of all of its neighbours. The parameter τ_{nem} should also be considered system-dependent, to be estimated by experiment. In our EDMD simulations of the quasi two-dimensional hard ellipsoid fluid, we find that τ_{nem} is approximately two orders of magnitude greater than the rotational timescale of a free ellipsoid τ_{visc} .

However, a limitation of our model is that it is unlikely to accurately model interfaces with extremely high surface coverages due to the increasing possibility of ellipsoidal particles with orientations pointing out of the interface² as well as it being outside the range of validity of the entropy expression Eq. (12). Finally, there is a region around the isotropic-nematic phase transition where neither method presented above produces satisfactory results for the timescale τ_{rot} due to large critical fluctuations near the transition.

We note that in comparison to the previous Section, where we had to run the simulation over a timespan longer than the longest timescale in the system in order to extract τ_{rot} , in this Section we see that exploiting thermodynamics results in computational efficiencies of several orders of magnitude. This is thanks to the fact that we need only simulate up to the intermediate timescale τ_s , which satisfies $\tau_s \ll \tau_{\text{rot}}$, especially for high surface coverages, when collective rearrangements are slow.

4 Discussion of the model

The closed set of time evolution equations describing our model is obtained from the four building blocks assembled

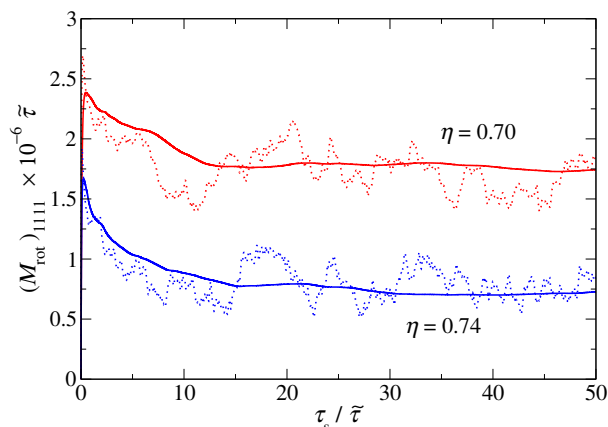


Fig. 3 Typical form of the $(M_{\text{rot}})_{1111}$ matrix entry calculated using Eq. (23) for $\eta = 0.70$ (dotted red line) and for $\eta = 0.74$ (dotted blue line). The solid lines are the $(M_{\text{rot}})_{1111}$ matrix entry calculated using Eq. (42). The correlation functions used to calculate these results were obtained with a moving window over a time series $0 < t < 200$ with timestep $dt = 0.001$ and then further averaged over 20 independent initial configurations.

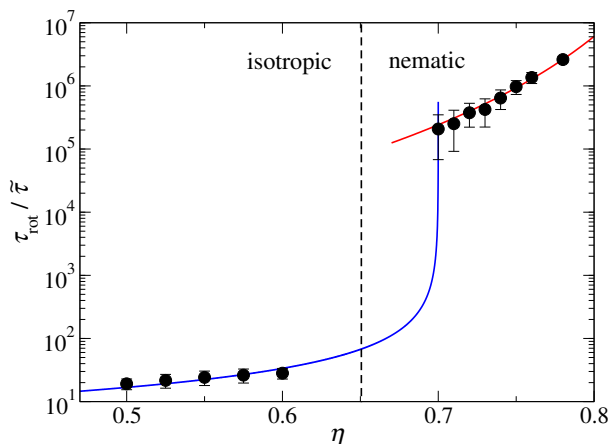


Fig. 4 Results for the rotational timescale τ_{rot} for the isotropic and nematic phases. The solid blue line (red solid line) is the power law fit in the isotropic (nematic) phase. The approximate packing fraction where the isotropic-nematic transition takes place is indicated by the dashed black line. Note the use of a logarithmic scale on the y -axis showing the significant increase of τ_{rot} across the isotropic-nematic transition.

according to Eq. (2), and reads

$$\dot{\rho} = -\frac{\partial}{\partial \mathbf{r}} \cdot (\rho \mathbf{v}) \quad (28)$$

$$\dot{\mathbf{M}} = -\frac{\partial}{\partial \mathbf{r}} \cdot (\mathbf{v} \mathbf{M}) - \frac{\partial}{\partial \mathbf{r}} \cdot \mathbf{s}_{\text{tot}} \quad (29)$$

$$\dot{u} = -\frac{\partial}{\partial \mathbf{r}} \cdot (u \mathbf{v}) - \mathbf{s} : \boldsymbol{\kappa}^T + 2\varepsilon_s \dot{\gamma} : \dot{\gamma} + \varepsilon_d (\text{tr} \dot{\gamma})^2 \quad (30)$$

$$\dot{\eta} = -\frac{\partial}{\partial \mathbf{r}} \cdot (\eta \mathbf{v}) \quad (31)$$

$$\dot{\mathbf{C}} = \boldsymbol{\kappa} \cdot \mathbf{C} + \mathbf{C} \cdot \boldsymbol{\kappa}^T - \mathbf{v} \cdot \frac{\partial \mathbf{C}}{\partial \mathbf{r}} - 2\mathbf{C} : \boldsymbol{\kappa}^T \mathbf{C} - \frac{1}{\tau_{\text{eff}}} (\mathbf{C} - \frac{1}{2} \boldsymbol{\delta}) \quad (32)$$

We have in Eq. (28) a statement of mass conservation, Eq. (29) contains the momentum balance terms, where the total surface stress is defined as

$$\mathbf{s}_{\text{tot}} = -\gamma \boldsymbol{\delta} + \boldsymbol{\Pi} + (\varepsilon_d - \varepsilon_s) \left(\frac{\partial}{\partial \mathbf{r}} \cdot \mathbf{v} \right) \boldsymbol{\delta} + 2\varepsilon_s \dot{\gamma}. \quad (33)$$

The total surface stress is the sum of entropic contributions to the stress and viscous terms. There is no energetic contribution because in our model, the particles only have excluded volume interactions. If there were other particle-particle interactions, these would be represented by a configurational internal energy density $u_c(\eta, \mathbf{C})$ term in the energy functional Eq. (8). In addition, there would also be an additional energetic contribution to the stress due to the structural variables.¹⁵

The internal energy time evolution Eq. (30) has the usual convection term and two sources: stress and viscous heating. The first of the structural variables η has in its time evolution Eq. (31) a conservation law. The second structural variable \mathbf{C} is upper convected, with the third term on the right hand side of Eq. (32) required to keep the trace of \mathbf{C} constant. For our model, we find a relaxation term with effective time constant

$$\frac{1}{\tau_{\text{eff}}} = f(\eta, S_2)(S_4 - 1) \frac{1}{\tau_{\text{rot}}}. \quad (34)$$

An interesting consequence of such an expression for the effective time constant is that rotational relaxation is hindered both by ordering from the factor $f(\eta, S_2)(S_4 - 1)$ as well as the caging effect of neighbouring particles intrinsic to the rotational timescale τ_{rot} . Recall that $f(\eta, S_2)$ is given in Eq. (16). The remarkable occurrence of only a linear (in $\mathbf{C} - \frac{1}{2} \boldsymbol{\delta}$) relaxation term in Eq. (32) is due to the two-dimensional nature of our system, where the tensor \mathbf{C} only has a single tensorial invariant. However, the effective time constant τ_{eff} is of course nonlinear in S_2 and η .

In comparison with the earlier model²⁰ we have corrected the upper convected behaviour of the tensor variable \mathbf{C} so that the trace is preserved. This leads to a modification of the anisotropic part of the surface stress Eq. (20). Also, we use an expression for the free energy that is accurate over a wider range of surface coverages, in particular across the isotropic-nematic transition.²¹

To study the fundamental physical behaviour of our model for often-used experimentally imposed flow conditions, we began with a number of simplifications, namely homogeneity of the particle area fraction, temperature, mass density and surface tension. Therefore the relevant state variables are reduced to the structural variables η and \mathbf{C} . For numerical solutions to the model equations, we must specify certain parameter values, which are summarised here: interfacial area removed per particles $A_p = 10^{-14} \text{m}^2$, temperature $T = 290 \text{K}$, rotational timescales $\tau_{\text{visc}} = 1 \text{s}$ and $\tau_{\text{nem}} = 10^2 \text{s}$, shear viscosity $\varepsilon_s = 10^{-8} \text{Pa m s}^{-1}$ corresponding to a water-air interface³⁴ and we assume for the dilational viscosity $\varepsilon_d = \varepsilon_s$. For dilational flow, where the surface coverage can vary through the isotropic-nematic phase transition, we need a way to smoothly describe the transition of the rotational timescale. In our numerical solutions, we use a simple method by finding the intercept between isotropic and nematic τ_{rot} ; for η below the intercept we use the isotropic fitting parameter (η_I) in the expression for τ_{rot} , while for η greater than the intercept we use the nematic fitting parameters (β, η_{max}). In the following, we use the inbuilt Matlab (Version 8.3, ode15) solver to numerically solve the set of differential equations. Initial conditions are always the equilibrium state for the initially assigned surface coverage.

4.1 Linear viscoelastic behaviour

Begin by examining the linear viscoelastic behaviour of our model for a general flow. The velocity gradient tensor can be written as $\boldsymbol{\kappa} = \boldsymbol{\kappa}_0 e^{i\omega t}$, where ω is the angular frequency of an oscillating flow. The response of the orientation tensor is then $\mathbf{C} = \mathbf{C}_0 + \mathbf{A} e^{i\omega t}$, where \mathbf{C}_0 is the orientation tensor at equilibrium and \mathbf{A} is a perturbation. Let us assume that the equilibrium state is isotropic so that $\mathbf{C}_0 = \boldsymbol{\delta}/2$. Substitution of these two expressions into Eq. (32) and neglecting second and higher order terms gives

$$\mathbf{A} = \frac{1}{i\omega + 1/\tau} \mathbf{S} = \mathbf{A}' - i\mathbf{A}'', \quad (35)$$

where we recall τ is the rotational relaxation timescale in the limit of zero ordering and \mathbf{S} is the two-dimensional deviatoric rate of deformation tensor

$$\mathbf{S} = \frac{1}{2} [\boldsymbol{\kappa}_0 + \boldsymbol{\kappa}_0^T - \text{tr}(\boldsymbol{\kappa}_0^T) \boldsymbol{\delta}].$$

The corresponding stress response is

$$\mathbf{\Pi} = -2k_B T n_p f(\eta, S_2 \rightarrow 0) [\mathbf{A}' \cos(\omega t) + \mathbf{A}'' \sin(\omega t)], \quad (36)$$

which is simply the Maxwell model of linear viscoelasticity with an effective number density $-n_p f(\eta, S_2 \rightarrow 0)$ (note that the function $f(\eta, S_2)$ is negative for $\eta < \eta_{in}$ and our above analysis is only valid for this range of surface coverages).

4.2 Steady simple shear

We present numerical results for start-up of simple shear for a wide range of shear rates in Figure 5, where the linear regime may no longer be accurate. We specialise Eq. (32) to the case of steady shear, where $(\boldsymbol{\kappa})_{xy} = \dot{\gamma}$ with $\dot{\gamma}$ the shear rate, and the other components of $\boldsymbol{\kappa}$ are equal to zero. The set of equations we numerically solve reads

$$\dot{C}_{xx} = 2\dot{\gamma} C_{xy} (1 - C_{xx}) - \frac{1}{\tau_{\text{eff}}} (C_{xx} - \frac{1}{2}), \quad (37a)$$

$$\dot{C}_{xy} = \dot{\gamma} (1 - C_{xx} - 2C_{xy}^2) - \frac{1}{\tau_{\text{eff}}} C_{xy}, \quad (37b)$$

where due to the properties of \mathbf{C} , we also have that $C_{yx} = C_{xy}$ and $C_{yy} = 1 - C_{xx}$. The shear component of the total surface stress is

$$(\mathbf{s}_{\text{tot}})_{xy} = \varepsilon_s \dot{\gamma} - 4n_p k_B T f(\eta, S_2) C_{xy} (C_{xx} - C_{xx}^2 - C_{xy}^2). \quad (38)$$

For the higher dimensionless shear rates $\dot{\gamma} \tau_{\text{visc}} \gtrsim 1$ we observe mild stress overshoots. Unlike the model presented in Ref.²⁰, our properly convected structural tensor variable is well-behaved, even for large dimensionless shear rates $\dot{\gamma} \tau_{\text{visc}}$. Note that our use of the trace-preserving closure in Eq. (17) precludes any tumbling behaviour of the director in the steady state.^{35,36} The orientation strength can be interpreted as a competition between the tendency of the particles to align with the flow, and the tendency to relax to their equilibrium state, given by the maximum of the entropy $s_{\text{id}} + s_{\text{excl}}$.

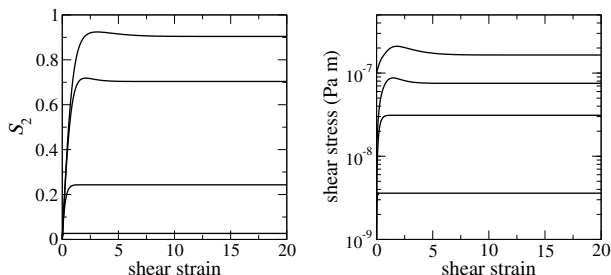


Fig. 5 Startup simple shear for surface coverage $\eta = 0.5$. From top to bottom are dimensionless shear rates of $\dot{\gamma} \tau_{\text{visc}} = 10, 1, 0.1, 0.01$.

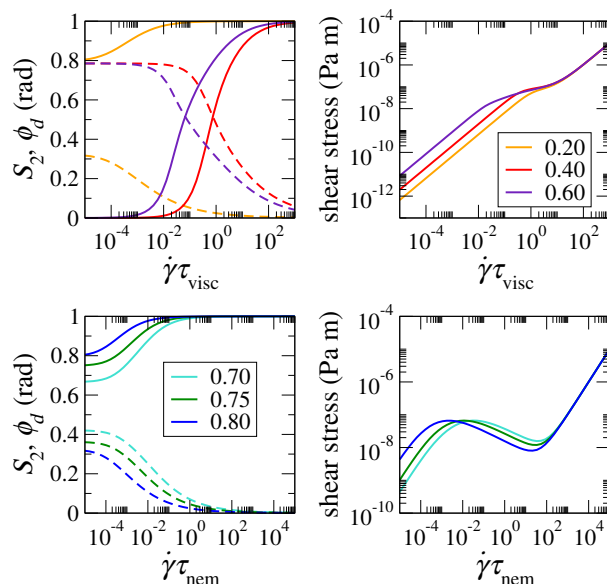


Fig. 6 Left panels. Steady state values of order parameter S_2 (solid lines), director angle with respect to the x -axis ϕ_d (dashed lines). Right panels. Shear stress plotted against a dimensionless shear rate for surface coverages indicated in the legend. Recall $\tau_{\text{visc}} = 1$ and $\tau_{\text{nem}} = 100$.

Flow curves calculated from steady state solutions of Eqs. (37) are shown in Figure 6. Increasing the shear rate results in increased ordering, and the director aligns more closely with the flow direction. From the total surface stress, we can define the effective surface shear viscosity, which takes into account the effect of adsorbed particles as $\varepsilon_s^{\text{eff}} = (\mathbf{s}_{\text{tot}})_{xy} / \dot{\gamma}$. We show the effective surface shear viscosity as a function of shear rate for a range of η in Figure 7.

There is a Newtonian regime at low shear rates, when the flow is not sufficiently strong to cause significant changes in the alignment. Shear-thinning behaviour is seen in Figure 7 for all surface coverages and is caused by ordering and the alignment of the director with the flow direction. In the limit of high shear rates, when the particles are perfectly ordered in the x -direction, they pose no further resistance to flow and we recover the viscosity of the bare interface.

When the surface coverage is sufficiently high *i.e.* $\eta > \eta_{in}$, we observe a mechanically unstable regime in the flow curves where the shear stress decreases with shear rate (see lower right panel of Figure 6), which would indicate shear banding behaviour. This behaviour is fairly widespread in complex fluids³⁷ and has been studied in various theoretical models of liquid crystal dynamics, which are similar to ours, see the review by Olmsted³⁸ and references therein. Typically, shear banding is attributed to strong shear-thinning caused by a large increase in alignment with a moderate increase in shear rate.

Our model would appear to support this explanation; the unstable area of the flow curve is precisely where shear-thinning is particularly pronounced. Although, recent numerical studies of various nematodynamic models including hydrodynamics, such as the study of Forest *et al.*³⁹ indicate shear banding is actually a rather delicate matter with a dynamic layering of time-dependent states.

We note that the other components of the of the stress tensor are non-zero, meaning that our model predicts a non-zero normal stress difference for steady in-plane shear of rigid anisotropic particles

$$(\mathbf{s}_{\text{tot}})_{xx} - (\mathbf{s}_{\text{tot}})_{yy} = 4k_{\text{B}}T f(\eta, S_2)(1 - 2C_{xx})(C_{xx}^2 + C_{xy}^2 - C_{xx}), \quad (39)$$

which vanishes when the system is in equilibrium thanks to the factor $f(\eta, S_2)$. Note that this normal stress difference is an in-plane and perpendicular to the direction of shear rather than out of plane.

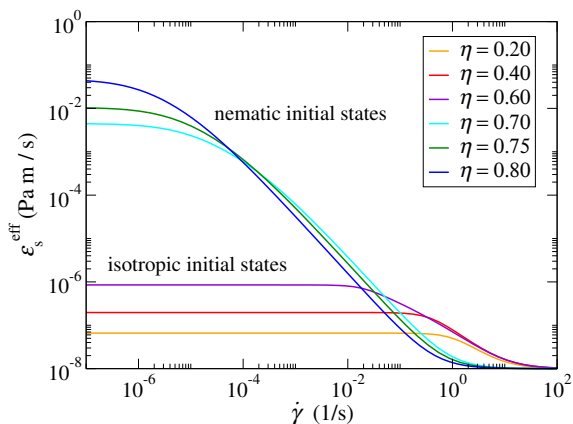


Fig. 7 The effective shear viscosity $\varepsilon_s^{\text{eff}}$ plotted as a function of shear rate for various packing fractions.

4.3 Oscillatory simple shear

Oscillatory simple shear has $(\boldsymbol{\kappa})_{xy} = \dot{\gamma}$ as the flow profile, with a time-dependent shear rate $\dot{\gamma}(t) = \gamma_0 \omega \cos \omega t$, where ω is the angular frequency and γ_0 is the maximum shear strain. The shear strain is defined as $\gamma = \gamma_0 \sin \omega t$. Again, surface area is conserved so that $\dot{\eta} = 0$. The set of equations is the same as Eqs. (37) and (38) but with a time dependent shear rate. In this case, the parameter space is increased to include the amplitude of shear γ_0 , and angular frequency ω .

There are typically three regimes related to the competition between shear-induced ordering and relaxation. The characteristic flow timescale is $\sim 2\pi/\omega$, while the effective rotational relaxation time is τ_{eff} . We show typical results for the

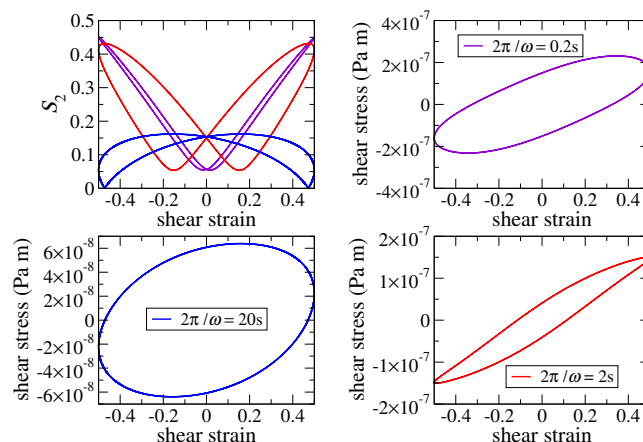


Fig. 8 Top left. Lissajous plot of ordering against the shear strain for $2\pi/\omega = 0.2\text{s}$ (violet), $2\pi/\omega = 2\text{s}$ (red) and $2\pi/\omega = 20\text{s}$ (blue). Clockwise, from top right. Lissajous stress-strain plots for $\eta = 0.4$, $\gamma_0 = 0.5$, and flow timescales $2\pi/\omega = 0.2, 2, 20\text{s}$. For this surface coverage, and taking into account the flow orientation, the effective rotational timescale is $\tau_{\text{eff}} \sim 1.1\text{s}$.

ordering and stress plotted against strain in Figure 8 for various angular frequencies covering a range of ratios between $\sim 2\pi/\omega$ and τ_{eff} . In the case where relaxation happens faster than the shear-induced ordering, the Lissajous stress-strain plots show purely viscous behaviour and flow-aligning behaviour is weak. More interesting behaviour is seen when both timescales are similar in value, then the stress-strain plots show a shear-thinning behaviour.

In Figure 9, we show ordering strength and shear stress Lissajous plots for two different surface coverages $\eta = 0.40$ (isotropic at equilibrium) and $\eta = 0.75$ (nematic at equilibrium). The stress-strain behaviour for both surface coverages is that of a purely viscous interface when γ_0 is small. As γ_0 increases, there is significant ordering and the contribution from the surface microstructure begins to be seen in the form of mild shear-thinning for $\eta = 0.40$ and in the form of shear-thickening for $\eta = 0.75$. We interpret this as being due to the fact that director is never in the optimal orientation with respect to the flow when the flow suddenly reverses.

We also present dynamic surface shear moduli for surface coverages in the isotropic phase in Figure 10. These are calculated by Fourier transforming the stress response $(\mathbf{s}_{\text{tot}})_{xy}$ and extracting the magnitude \hat{A} and phase lag δ of the first harmonic. The storage and loss moduli are then respectively defined as $G' = (\hat{A}/\gamma_0) \cos \delta$ and $G'' = (\hat{A}/\gamma_0) \sin \delta$.

The top panel of Figure 10 shows dynamic moduli for an inverse frequency $1/f \gg \tau_{\text{eff}}$. The bottom panel of Figure 10 contains shear amplitude sweeps in the case where $1/f \sim \tau_{\text{eff}}$. Here, we observe a greater range of behaviours for the different surface coverages. The lowest surface coverage $\eta = 0.4$,

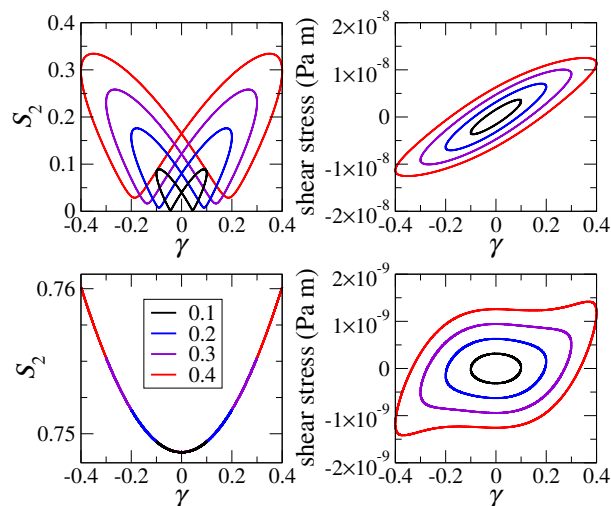


Fig. 9 *Left panels.* Plots of orientational strength as a function of shear strain. Top shows $\eta = 0.40$ and bottom shows $\eta = 0.75$. *Right panels.* Lissajous plots of the shear stress for angular frequency $\omega = 0.05 \times 2\pi \text{ rad s}^{-1}$. We vary the amplitude of the shear amplitude γ_0 according to the legend.

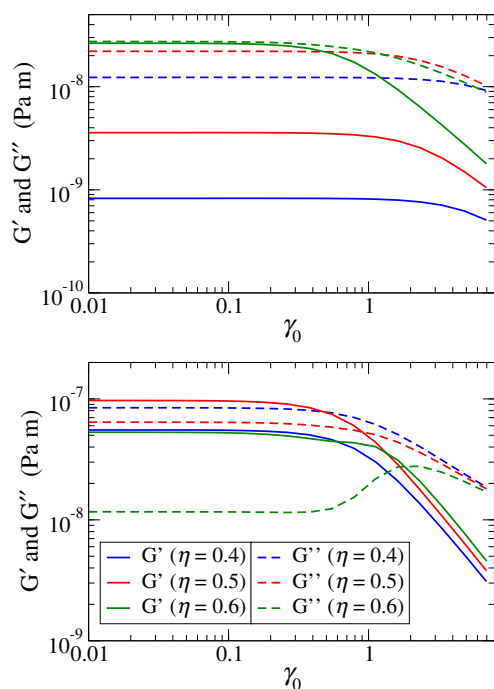


Fig. 10 *Top panel.* Dynamic shear moduli plotted against the shear amplitude for an angular frequency $\omega = 0.01 \times 2\pi \text{ rad s}^{-1}$. *Bottom panel.* Dynamic shear moduli plotted against the shear amplitude for a higher frequency $\omega = 0.1 \times 2\pi \text{ rad s}^{-1}$. Both graphs use the same legend.

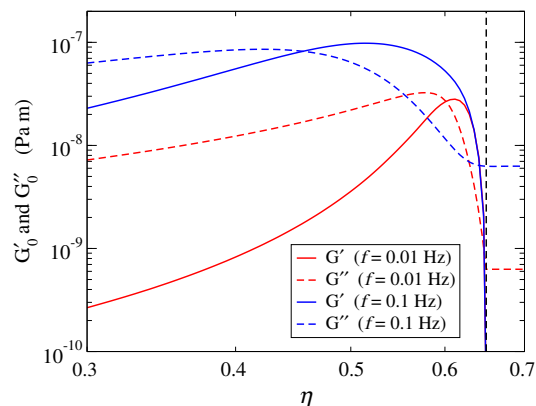


Fig. 11 Zero-shear amplitude limit of the dynamic shear moduli plotted against surface coverage for frequencies $f = 0.01 \text{ Hz}$ and $f = 0.1 \text{ Hz}$. Note that the dynamic dilatational moduli E'_0, E''_0 in the zero deformation amplitude limit are (in two dimensions) identical to G'_0, G''_0 .⁸ The vertical dashed line indicates η_{in} .

exhibits dominant viscous behaviour, while increasing the surface coverage to $\eta = 0.5$ leads to a more elastic interface for lower shear amplitudes. As the surface coverage is increased further to $\eta = 0.6$, the loss modulus shows non-monotonic behaviour, that is qualitatively similar to the dynamic moduli obtained experimentally with a monolayer of haematite ellipsoid-shaped particles of aspect ratio ~ 4.6 .²

The zero-shear limit of the dynamic moduli G'_0, G''_0 for a range of surface coverages and both frequencies is presented in Figure 11. The storage moduli is found to increase with surface coverage. We find power law behaviour for dilute surface coverages. The storage moduli peak just before η_{in} and drop to zero at the isotropic-nematic transition. The contribution to the interface elasticity comes from flow-induced ordering effects, which are very weak in the nematic phase $\eta > \eta_{in}$, when the particles are already ordered at equilibrium. For $\eta > \eta_{in}$, we would therefore only expect to see a loss modulus (in the limit $\gamma_0 \rightarrow 0$), which only has a contribution from the surface shear viscosity of the bare interface.

4.4 Oscillatory dilatational flow

We model the oscillating barrier method in a Langmuir trough. In this experimental technique, barriers oscillate along a single direction with angular frequency ω , causing the surface area A of the interface to vary in time, i.e. $A(t) = A_0(1 + \Gamma_0 \sin \omega t)$, where A_0 is the initial surface area and Γ_0 is the amplitude of deformation, measured as a fraction of A_0 . The velocity gradient of such a flow field is therefore given by $(\kappa)_{xx} = \Gamma_0 \omega \cos(\omega t) / (1 + \Gamma_0 \sin \omega t)$, with the other components equal to zero. Therefore, in terms of components of \mathbf{C} , the equations

of motion to solve are

$$\dot{C}_{xx} = 2(\kappa)_{xx}C_{xx}(1 - C_{xx}) - \frac{1}{\tau_{\text{eff}}}\left(C_{xx} - \frac{1}{2}\right), \quad (40a)$$

$$\dot{C}_{xy} = (\kappa)_{xx}C_{xy}(1 - 2C_{xx}) - \frac{1}{\tau_{\text{eff}}}C_{xy}. \quad (40b)$$

If we take an isotropic state as the initial condition, Eq. (40b) is identical to zero and we are left with a single equation to solve for C_{xx} . Note, however, that this is still a highly nonlinear equation due to the dependence of τ_{eff} on both η and S_2, S_4 .

Solution of the balance equation for the surface coverage Eq. (31) yields $\eta(t) = \eta(0)/(1 + \Gamma_0 \sin \omega t)$. Since the surface coverage varies, we must also take into account its contribution to the surface tension, see Eq. (19) so that the surface extra stress s_{ex} we measure is given by

$$s_{\text{ex}} = \Pi - \Delta\gamma \delta, \quad (41)$$

with the change in surface tension given by

$$\Delta\gamma = \eta T \frac{\partial s}{\partial \eta} - \left[\eta T \frac{\partial s}{\partial \eta} \right]_{t=0}.$$

Note that the number density of adsorbed particles n_p (used in the entropy densities $s_{\text{id}}, s_{\text{excl}}$) also varies in the same way as the surface coverage η .

In Figure 12 we show the time response of the xx -component of the surface extra stress defined in Eq. (41) to an oscillatory dilatational strain. The system parameters are $\eta = 0.4, \omega = 0.1 \times 2\pi \text{ rad s}^{-1}$ and strain amplitudes varying from 0.02 to 0.45. Increasing the strain amplitude Γ_0 results in the presence of higher harmonics in the stress response, which is manifested by an increasing deviation from purely sinusoidal behaviour.

The corresponding Lissajous plots of Figure 12 for the orientation tensor components and xx -component of the surface extra stress are displayed in Figure 13. As expected, in compression (when the strain is negative), the particles tend to align in the y -direction, while in extension (when the strain is positive), the particles tend to align in the x -direction. For small strain amplitudes (see $\Gamma_0 = 0.02$ in Figure 13), the effective relaxation time τ_{eff} changes only a little so the magnitude of flow-induced ordering is approximately symmetric in the compression and extension phases. Therefore the Lissajous plot of the stress shows no nonlinear behaviour. Upon increasing the strain amplitude, the surface coverage increases in the compression phase, with a corresponding increase in τ_{eff} . Relaxation occurs more slowly here than in the extension phase. This effect is reflected in the increased flow-induced ordering in the compression phase compared with the extension phase. As a consequence of the ordering and increased surface coverage, the stress in the compression phase is significantly greater than in the extension phase. Increasing the

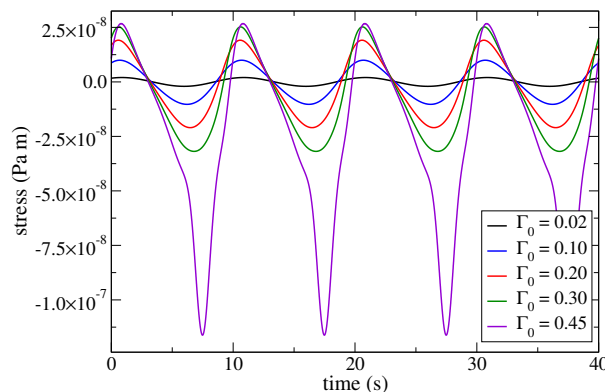


Fig. 12 Time response of the xx -component of the stress tensor to the applied oscillatory dilatational strain for a range of strain amplitudes Γ_0 . Note that the maximum surface coverage achieved in the compression phase for $\Gamma_0 = 0.45$ is approximately 0.73. The corresponding Lissajous plots are shown in Figure 13.

strain amplitude even further, we find a sudden and significant resistance to compression due to the particles approaching a jammed state, see bottom panel in Figure 13. The behaviour seen in our macroscopic rheological model for dilatational flow illustrate the importance of a rotational relaxation time and entropy that varies in the correct way with η and S_2 .

The dynamic surface dilatational storage and loss moduli E' and E'' for the same numerical parameters as above are shown in Figure 14. Similarly to the dynamic shear moduli, E' and E'' are calculated by Fourier transforming the stress response $(s_{\text{ex}})_{xx}$ and extracting the magnitude \tilde{A} and phase lag δ of the first harmonic. The dilatational storage and loss moduli are then respectively defined as $E' = (\tilde{A}/\Gamma_0) \cos \delta$ and $E'' = (\tilde{A}/\Gamma_0) \sin \delta$. For small strain amplitudes the interface is mostly viscous, however, elastic behaviour dominates when the particles in the interface approach a high surface coverage in the compression part of the flow. The compression also leads to a rapid increase of the storage modulus E' for high strain amplitudes, as the particles approach a jammed state, where they exhibit a greater resistance to compression, which is also seen in the high strain amplitude Lissajous plots of Figure 13.

5 Concluding remarks and outlook

In this paper, we provide not only the tools, but also demonstrate for a simple example, how to derive macroscopic constitutive equations for the interfacial rheology of complex fluid-fluid interfaces. For the demonstration of our approach, we begin with a well-defined microscopic model of hard ellipsoids confined to a plane. We show the advantage of exploiting thermodynamics to efficiently bridge timescales when

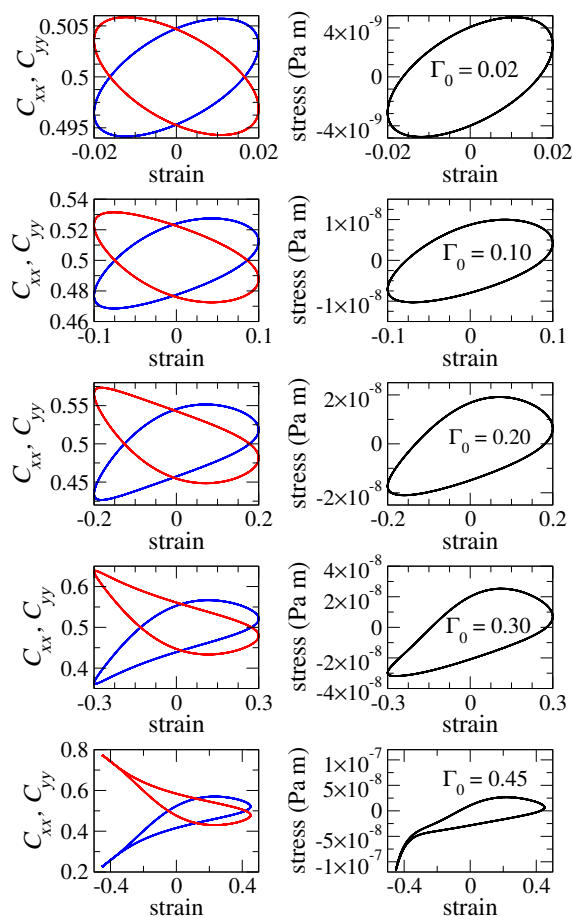


Fig. 13 Dilatational rheology for initial surface coverage $\eta(0) = 0.40$ and $\omega = 0.1 \times 2\pi \text{ rad s}^{-1}$. *Left column.* Lissajous plots of orientation tensor components C_{xx} (blue) and C_{yy} (red) against the strain defined as $(A(t) - A_0)/A_0$ for various area deformation amplitudes from the top $\Gamma_0 = 0.02, 0.10, 0.20, 0.30, 0.45$. *Right column.* Lissajous figure of the xx -component of the stress plotted against the strain for the same deformation amplitudes as listed above.

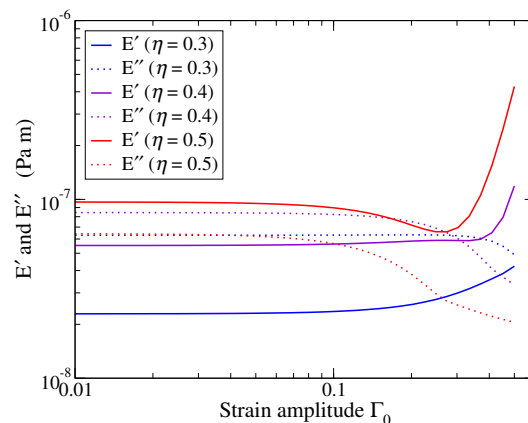


Fig. 14 A strain sweep of the dynamic moduli for $\eta(0) = 0.3, 0.4, 0.5$ and $\omega = 0.1 \times 2\pi \text{ rad s}^{-1}$. Note the rapid increase in elastic modulus as higher surface coverages are reached by increasing the strain amplitude.

we extract the long rotational timescale from short time simulations for high surface coverages. The macroscopic constitutive equations formulated with the aid of nonequilibrium thermodynamics, clearly establish the important relationships between surface structure and various timescales in different flow conditions. Accurately modelling these relationships is shown to be crucial to understanding the interfacial rheology of particle-stabilised fluid interfaces and reproducing the rich variety of behaviours seen in experiments.^{2,4}

The general nature of our approach (based on systematic coarse-graining and the nonequilibrium thermodynamic framework GENERIC) can be readily applied to derive reliable constitutive equations for other specific systems of interest, once sufficiently detailed microscopic models of these systems are developed.

Acknowledgements

AML is grateful to Wensheng Xu for sending his raw data on the diffusion constants for hard ellipses and would also like to thank Pavlos S. Stephanou for a stimulating discussion on this manuscript.

Appendix: Orientational relaxation of rotators by Brownian motion

Here we present the calculations leading to our theoretical result for the friction matrix entry for rotational relaxation Eq. (24). Begin with the microscopic expression for the fric-

tion matrix entry¹⁵, which is the integrated version of Eq. (23),

$$M_{\text{rot}} = \frac{A}{2k_B\tau_s} \langle \Delta_{\tau_s} \mathbf{C}(z) \Delta_{\tau_s} \mathbf{C}(z) \rangle, \quad (42)$$

where A is the surface area of the system, $\langle \dots \rangle$ denotes an average over an ensemble of atomistic trajectories consistent with a given coarse-grained state, $\Delta_{\tau_s} \mathbf{C}(z) = \mathbf{C}(z(\tau_s)) - \mathbf{C}(z(0))$ is the incremental change of \mathbf{C} over the time τ_s and z are the atomistic variables. Since we are only interested in rotation, $z = \{\mathbf{u}_1, \dots, \mathbf{u}_N\}$, the set of orientation vectors. The time τ_s is an intermediate timescale separating the slow from the fast dynamics. If we assume that τ_s is sufficiently small such that there is no systematic change of an ellipse orientation \mathbf{u} over the timescale τ_s , then any changes of \mathbf{u} are due to noise, which we model with a stochastic differential equation in the Itô prescription⁴⁰

$$\mathbf{u}(\tau_s) - \mathbf{u}(0) = -\frac{1}{2}B^2\tau_s\mathbf{u}(0) + B[\boldsymbol{\delta} - \mathbf{u}(0)\mathbf{u}(0)] \cdot \Delta\mathbf{W}, \quad (43)$$

where $B = \sqrt{2k_B T/\zeta}$ is the noise amplitude of the two-dimensional Wiener process with friction coefficient ζ and $\Delta\mathbf{W} = \mathbf{W}(\tau_s) - \mathbf{W}(0)$ is a Wiener increment. Note that the stochastic dynamics of Eq. (43) preserves the normalisation $\mathbf{u}^2 = 1$. We can actually neglect the first term on the right hand side of Eq. (43) since it only contributes second and higher order terms in $(\tau_s/\tau_{\text{rot}})$ in the correlation function of Eq. (42). The quantity $\Delta_{\tau_s} \mathbf{C}(z)$ can thus be written

$$\Delta_{\tau_s} \mathbf{C}(z) = B\mathbf{u}(\boldsymbol{\delta} - \mathbf{u}\mathbf{u}) \cdot \Delta\mathbf{W} - \overline{(\boldsymbol{\delta} - \mathbf{u}\mathbf{u}) \cdot \Delta\mathbf{W} \mathbf{u}}, \quad (44)$$

where it is understood that $\mathbf{u} = \mathbf{u}(0)$, $\overline{\mathbf{X}} = \sum_{i=1}^N \mathbf{X}_i/N$ denotes the mean of \mathbf{X} and terms of order $(\Delta\mathbf{W})^2$ have been neglected. Note the ordering of the tensor products and the contractions. Substitution of Eq. (44) into Eq. (42) yields the following

$$M_{\text{rot}} = \frac{B^2}{2k_B\tau_s n_p} \langle \overline{\mathbf{u}\mathbf{A}\mathbf{u}\mathbf{A}} + \overline{\mathbf{A}\mathbf{u}\mathbf{u}\mathbf{A}} + \overline{\mathbf{A}\mathbf{u}\mathbf{A}\mathbf{u}} + \overline{\mathbf{u}\mathbf{A}\mathbf{A}\mathbf{u}} \rangle, \quad (45)$$

where we have abbreviated the vector $\mathbf{A} = (\boldsymbol{\delta} - \mathbf{u}\mathbf{u}) \cdot \Delta\mathbf{W}$ and $n_p = N/A$ is the number density of adsorbed particles. After some algebraic manipulations and noting that $\langle \Delta\mathbf{W}\Delta\mathbf{W} \rangle = \tau_s\boldsymbol{\delta}$ along with the definition $\mathbf{C} = \overline{\mathbf{u}\mathbf{u}}$ we find that

$$(M_{\text{rot}})_{ijkl} = \frac{B^2}{2k_B n_p} (C_{ik}\delta_{jl} + C_{jk}\delta_{il} + C_{jl}\delta_{ik} + C_{il}\delta_{jk} - 4(C_4)_{ijkl}), \quad (46)$$

which is the theoretical expression for the friction matrix entry written in Eq. (24). We identify the friction coefficient with

the rotational timescale $\zeta = \tau_{\text{rot}}/k_B T$ to recover Eq. (24). Note that the fourth moment $\mathbf{C}_4 = \langle \mathbf{u}\mathbf{u}\mathbf{u}\mathbf{u} \rangle$ appears due to the constraint of constant length. The fourth moment can be expressed exactly in terms of the second moment and the identity tensor. From symmetry considerations \mathbf{C}_4 can be decomposed into

$$(C_4)_{ijkl} = S_4 n_i n_j n_k n_l + X(n_i n_j \delta_{kl} + 5 \text{ perms.}) + Y(\delta_{ij} \delta_{kl} + 2 \text{ perms.}), \quad (47)$$

where perms. indicates additional all permutations of the indices and \mathbf{n} is the director, which is the eigenvector associated with the greatest eigenvalue of \mathbf{C} and indicates the direction of ordering. The coefficients X, Y are uniquely determined by the following properties of the second and fourth moment

$$(C_4)_{ijkk} = C_{ij} \quad \text{and} \quad C_{ii} = 1, \quad (48)$$

which when combined with the relationship

$$C_{ij} = S_2 n_i n_j + \frac{1}{2}(1 - S_2)\delta_{ij}, \quad (49)$$

yields

$$X = \frac{S_2 - S_4}{6} \quad \text{and} \quad Y = \frac{3 + S_4 - 4S_2}{24}. \quad (50)$$

One can then convert Eq. (47) to be in terms of \mathbf{C} and $\boldsymbol{\delta}$ rather than \mathbf{n} and $\boldsymbol{\delta}$. Finally the order parameter S_4 is expressed in terms of S_2 using the generalised canonical ensemble. The distribution function f for two-dimensional non-interacting rotators is

$$f = \frac{1}{Z} \exp[-\boldsymbol{\Lambda} : (\mathbf{u}\mathbf{u} - \boldsymbol{\delta}/2)] \quad (51)$$

where $\boldsymbol{\Lambda}$ is the Lagrange multiplier, which we can choose to be $\Lambda_{11} = -\Lambda_{22} = \lambda$ without loss of generality and $Z = I_0(\lambda)$ is the partition function; I_n is a modified Bessel function of the first kind. The Lagrange multiplier sets the average orientation of the ensemble of rotators. Writing the orientation vector as $\mathbf{u} = (\cos\theta, \sin\theta)$ we can calculate the ensemble averages in order to obtain the order parameters

$$S_2 = \frac{1}{I_0(\lambda)} \int_0^{2\pi} \frac{d\theta}{2\pi} \cos(2\theta) e^{-\lambda \cos(2\theta)} = \frac{I_1(\lambda)}{I_0(\lambda)}, \quad (52)$$

$$S_4 = \frac{1}{I_0(\lambda)} \int_0^{2\pi} \frac{d\theta}{2\pi} \cos(4\theta) e^{-\lambda \cos(2\theta)} = \frac{I_2(\lambda)}{I_0(\lambda)}. \quad (53)$$

References

- 1 B. P. Binks and T. S. Horozov, *Colloidal Particles at Liquid Interfaces*, Cambridge University Press, 2006.
- 2 B. Madivala, S. Vandebriel, J. Fransaer and J. Vermant, *Soft Matter*, 2009, 5, 1717–1727.

- 3 J. C. Loudet, A. M. Alsayed, J. Zhang and A. G. Yodh, *Phys. Rev. Lett.*, 2005, **94**, 018301.
- 4 B. Madivala, J. Fransaer and J. Vermant, *Langmuir*, 2009, **25**, 2718–2728.
- 5 L. Botto, E. P. Lewandowski, M. Cavallaro and K. J. Stebe, *Soft Matter*, 2012, **8**, 9957–9971.
- 6 W. Ramsden, *Proceedings of the Royal Society of London*, 1903, **72**, 156–164.
- 7 S. U. Pickering, *J. Chem. Soc., Trans.*, 1907, **91**, 2001–2021.
- 8 L. M. C. Sagis, *Rev. Mod. Phys.*, 2011, **83**, 1367–1403.
- 9 F. Bresme and J. Faraudo, *J. Phys.: Condens. Matter*, 2007, **19**, 375110.
- 10 M. Oettel and S. Dietrich, *Langmuir*, 2008, **24**, 1425–1441.
- 11 M. Cavallaro, L. Botto, E. P. Lewandowski, M. Wang and K. J. Stebe, *PNAS*, 2011, **108**, 20923–20928.
- 12 L. M. C. Sagis and H. C. Öttinger, *Phys. Rev. E*, 2013, **88**, 022149.
- 13 P. A. Kralchevsky and K. Nagayama, *Adv. Colloid Interface Sci.*, 2000, **85**, 145 – 192.
- 14 G. B. Davies, T. Krüger, P. V. Coveney and J. Harting, *J. Chem. Phys.*, 2014, **141**, 154902.
- 15 H. C. Öttinger, *Beyond Equilibrium Thermodynamics*, Wiley–Interscience, New Jersey, 2005.
- 16 M. Grmela and H. C. Öttinger, *Phys. Rev. E*, 1997, **56**, 6620–6632.
- 17 H. C. Öttinger and M. Grmela, *Phys. Rev. E*, 1997, **56**, 6633–6655.
- 18 H. C. Öttinger, *MRS Bulletin*, 2007, **32**, 936–940.
- 19 T. Savin, K. S. Glavatskiy, S. Kjelstrup, H. C. Öttinger and D. Bedeaux, *Europhys. Lett.*, 2012, **97**, 40002.
- 20 L. M. C. Sagis, *Phys. Rev. E*, 2013, **88**, 022150.
- 21 A. M. Luo, L. M. C. Sagis and P. Ilg, *J. Chem. Phys.*, 2014, **140**, 124901.
- 22 P. Ilg, *Phys. Rev. E*, 2012, **85**, 061709.
- 23 A. Beris and B. J. Edwards, *Thermodynamics of Flowing Systems: With Internal Microstructure*, Oxford University Press, 1994.
- 24 B. J. Edwards, A. N. Beris and M. Grmela, *Mol. Cryst. Liq. Cryst.*, 1991, **201**, 51–86.
- 25 M. Doi and T. Ohta, *J. Chem. Phys.*, 1991, **95**, 1242–1248.
- 26 B. J. Edwards and H. C. Öttinger, *Phys. Rev. E*, 1997, **56**, 4097–4103.
- 27 M. Doi and S. F. Edwards, *The Theory of Polymer Dynamics*, Oxford University Press, 1986.
- 28 P. Ilg and M. Kröger, *J. Rheol.*, 2011, **55**, 69–93.
- 29 P. Ilg, H. C. Öttinger and M. Kröger, *Phys. Rev. E*, 2009, **79**, 011802.
- 30 C. De Michele, *Journal of Computational Physics*, 2010, **229**, 3276 – 3294.
- 31 A. N. Lagar'kov and V. H. Sergeev, *Sov. Phys. Usp.*, 1978, **21**, 566.
- 32 P. Español and I. Ziga, *J. Chem. Phys.*, 1993, **98**, 574–580.
- 33 J. Pach and P. K. Agarwal, *Combinatorial Geometry*, Wiley-Interscience, 1995.
- 34 J. C. Earnshaw, *Nature*, 1981, **292**, 138–139.
- 35 A. N. Semenov, *Zh. Eksp. Teor. Fiz.*, 1983, **85**, 549–560.
- 36 N. Kuzuu and M. Doi, *J. Phys. Soc. Jpn.*, 1983, **52**, 3486–3494.
- 37 G. Ovarlez, S. Rodts, X. Chateau and P. Coussot, *Rheol. Acta*, 2009, **48**, 831–844.
- 38 P. D. Olmsted, *Rheol. Acta*, 2008, **47**, 283–300.
- 39 M. G. Forest, S. Heidenreich, S. Hess, X. Yang and R. Zhou, *J. Non-Newton. Fluid.*, 2010, **165**, 687–697.
- 40 H. C. Öttinger, *Stochastic Processes in Polymeric Fluids*, Springer, 1996.